Journal of
Mechanics of
Materials and Structures

COMPARISON OF SERIES AND FINITE DIFFERENCE SOLUTIONS TO REMOTE TENSILE LOADINGS OF A PLATE HAVING A LINEAR SLOT WITH ROUNDED ENDS

David J. Unger

Volume 15, No. 3 May 2020

msp

JOURNAL OF MECHANICS OF MATERIALS AND STRUCTURES
Vol. 15, No. 3, 2020
https://doi.org/10.2140/jomms.2020.15.361

COMPARISON OF SERIES AND FINITE DIFFERENCE SOLUTIONS TO REMOTE TENSILE LOADINGS OF A PLATE HAVING A LINEAR SLOT WITH ROUNDED ENDS

DAVID J. UNGER

Plane stress linear elastic solutions are obtained for a straight slot with rounded ends subject to remotely applied tensile tractions. The series solutions are obtained using a Kolosov–Muskhhelishvili complex variable approach together with an expansion technique developed extensively by G. N. Savin. The finite difference solutions employ an orthogonal curvilinear coordinate system and simulate loads applied at infinity using finite boundaries that are large in comparison to the slot length. The slot shape is similar to the geometry found in the D. Riabouchinsky free streamline problem for fluid flow around two flat plates. Both uniaxial loadings normal to the slot and uniform biaxial loadings are examined.

1. Introduction

The problems addressed in this paper are similar to mode I crack problems [Unger 2011] found in linear elastic fracture mechanics. Unlike crack problems, the conformal mapping of a slot onto a unit circle to facilitate solution involves the use of a transcendental function. However, the most powerful analytical solution technique known for solving plane linear elastic problems limits the mapping function to be at most a rational function of the mapping variable in order to guarantee solution [Muskhelishvili 1977]. The traditional way to avoid this problem is to use a power series expansion of an algebraic or transcendental function in terms of the transformation variable of the mapping function [Savin 1961]. This is the technique employed here.

Once a proper conformal mapping function is identified, a numerical finite difference scheme can also be formulated using the orthogonal curvilinear coordinates defined by the conformal mapping or one that is closely related to it. However, use of a series expansion as a solution technique often generates oscillatory behavior in the solution even after many terms of the expansion are retained including those utilizing modern optimization techniques of the genetic-algorithm variety [Vigdergauz 2006]. This can make the determination of the largest principal stress problematic and consequently the stress concentration factor. The use of a finite difference solution scheme for comparison helps verify the maximum value of the principal stress as numerical solutions of this type are not prone to oscillations.

A summary of classical stress concentration factors for holes of various types in plates for linear elastic behavior may be found in the most currently revised edition of Peterson's handbook [Pilkey et al. 2020]. A large compilation of stress concentration factor literature for analyses conducted after 1974 appears in [Hardy and Malik 1992]. Another relatively recent reference on stress concentration factors is [Savruk and Kazberuk 2017].

Keywords: stress concentration factor, Riabouchinsky free streamline problem.

One motivation for this analysis is that fracture mechanics specimens require a straight slot of finite width be cut into a plate before a fatigue crack can be generated at the tip of the slot. The knowledge of the stress concentration factor due to the slot itself helps quantify the overall state of stress into which the crack propagates [Collins 1993; Rice 1988].

Typically, linear elastic solutions of slots of finite widths are often approximated by use of elongated elliptical hole or parabolic notch analyses [Tada et al. 2000; Creager and Paris 1967]. Nevertheless, there can be large discrepancies between the predictions of linear elastic solutions for elongated ellipses and notches and those of finite-width slots. This can be readily discerned for a mode III slot problem of this shape [Unger 2012a; 2012b], which has a closed-form solution, and those of an ellipse [Neuber 2001] with a similar aspect ratio of semimajor to semiminor axes.

2. Series solution of the slot problem

The mapping function of a plane exterior to a slot geometry of the type shown in Figure 1 onto the interior of a unit circle is [Unger 2016; 2018]

$$z=\omega(\zeta)=\frac{a}{2}\left\{-(1-k_1)\frac{1+\zeta^2}{2\zeta}+\operatorname{sgn}(\operatorname{Re}\zeta)[k_1K(m)-E(m)]\right.$$
$$\left.+i(1+k_1)\left[E\left(\sin^{-1}\frac{i}{k_2}\frac{1-\zeta^2}{2\zeta},k_2^2\right)-\frac{(1-k_1)^2}{(1+k_1)^2}F\left(\sin^{-1}\frac{i}{k_2}\frac{1-\zeta^2}{2\zeta},k_2^2\right)\right]\right\}, \tag{1}$$

where the various parameters of the elliptic integrals [Abramowitz and Stegun 1964] of (1) are defined by

$$m=1-m_1,\quad k_1=\sqrt{m_1},\quad k_2=\frac{2\sqrt{k_1}}{1+k_1},\quad 0\le m_1\le 1 \tag{2}$$

and a is a scaling parameter with units of length.

The aspect ratio A_R of total slot length to the total slot width is [Unger 2016]

$$A_R=\frac{1-\sqrt{m_1}(K(m)+1)+E(m)}{2[E(m_1)-(1-\sqrt{m_1})K(m_1)]}. \tag{3}$$

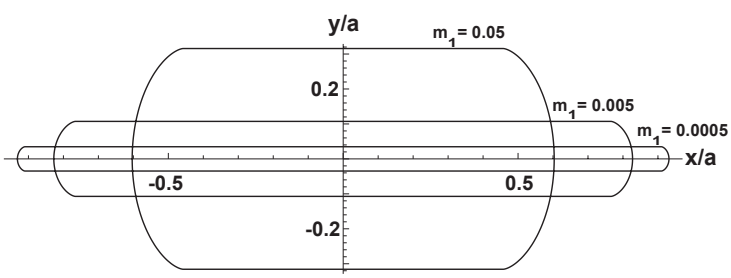

Figure 1. Variation of slot aspect ratio and shape with elliptic integral parameter.

The curved tip at the right-hand side of the slot has the following parametric relationship [Unger 2019] with θ in Cartesian coordinates $z = x + iy$:

$$x_{\text{tip}} = \frac{a}{2}[(1-k_1)\cos\theta - k_1 K(m) + E(m)], \quad -\frac{\pi}{2} \le \theta \le \frac{\pi}{2},$$
$$y_{\text{tip}} = \frac{a}{2}(1+k_1)\left[E\left(\sin^{-1}\left(\frac{\sin\theta}{k_2}\right), k_2^2\right) - \frac{(1-k_1)^2}{(1+k_1)^2}F\left(\sin^{-1}\left(\frac{\sin\theta}{k_2}\right), k_2^2\right)\right], \quad \text{for } -\frac{\pi}{2} \le \theta \le \frac{\pi}{2}, \tag{4}$$

where θ is the angle of the polar representation of the transform variable ζ

$$\zeta = \rho\exp(i\theta), \quad 0 \le \rho \le 1, \quad -\pi \le \theta \le \pi, \tag{5}$$

and where ρ is the radius.

This shape was first obtained in connection with the solution of the free streamlines of an ideal fluid flowing past two side-by-side flat plates [Riabouchinsky 1921]. An analogy with the antiplane slot problem was investigated in detail in [Unger 2018; 2019]. Note that the slot tip will actually change shape slightly with m_1 in Figure 1, but it does so almost imperceptibly for small changes in this parameter. As $m_1 \to 0$, the slot tip shape approaches asymptotically that of a cycloid [Unger 2018]. This particular shape was chosen for the slot as it provides a single analytical expression for a smooth transition from its flat surfaces to its rounded ends. This is an important attribute when solving the problem analytically. In contrast, the ovaloid, which is a slot shape composed of flat surfaces connected by semicircular ends, requires two different meshes composed individually of Cartesian and polar coordinates for solution [Bowie and Freese 1978].

Let us perform a series expansion of $z(\zeta)$ of (1) about the point ζ equals zero retaining only the first three terms of the series

$$z(\zeta) = -\frac{a}{2\zeta} + \frac{a(3m_1^{1/2}-1)\zeta}{2(m_1^{1/2}+1)} + \frac{2am_1^{1/2}(m_1^{1/2}-1)^2\zeta^3}{3(m_1^{1/2}+1)^3} + \cdots. \tag{6}$$

Note that if one wishes to expand this series beyond the three terms shown, using the symbolic software Mathematica, it may be easier to first differentiate $z(\zeta)$ of (1) with respect to ζ and then expand the derivative. This would be followed by integrating the resulting series of the derivative with respect to ζ to obtain the series expansion of $z(\zeta)$.

The symbol σ is traditionally used to represent ζ on the surface of the unit circle where ρ of (5) equals one:

$$\sigma = \exp(i\theta). \tag{7}$$

Similarly, $z(\zeta)$ on the unit circle γ is traditionally represented by the symbol $\omega(\sigma)$ such that (6) becomes

$$\omega(\sigma) = -\frac{a}{2\sigma} + \frac{a(3m_1^{1/2}-1)\sigma}{2(m_1^{1/2}+1)} + \frac{2am_1^{1/2}(m_1^{1/2}-1)^2\sigma^3}{3(m_1^{1/2}+1)^3} + \cdots. \tag{8}$$

Now one of the complex functions that is used in a Muskhelishvili solution scheme is a function designated as $\varphi(\zeta)$. Following the series expansion technique developed in [Savin 1961], one decomposes the

function $\varphi(\zeta)$ for a remote tensile traction T_∞ applied along a single axis by

$$\varphi(\zeta) = T_\infty\, z(\zeta)/4 + \varphi_0(\zeta), \tag{9}$$

where the following integral equation must be solved:

$$\varphi_0(\zeta) + \frac{1}{2\pi i}\int_\gamma \frac{\omega(\sigma)}{\overline{\omega'(\sigma)}}\overline{\varphi_0'(\sigma)}\frac{d\sigma}{\sigma-\zeta} = \frac{1}{2\pi i}\int_\gamma (f_1^0 + i f_2^0)\frac{d\sigma}{\sigma-\zeta}. \tag{10}$$

The bar above a variable in (10) represents the complex conjugate of a related function without the bar. Part of the integrand on the right-hand side of (10) is given by

$$f_1^0 + i f_2^0 = -\frac{T_\infty}{2}[\omega(\sigma) - \exp(2i\alpha)\,\overline{\omega(\sigma)}], \tag{11}$$

where α represents an angle in the direction of the applied traction at infinity T_∞. Now the complex conjugate of $z(\zeta)$ is given by

$$\bar{z}(\bar{\zeta}) = -\frac{a}{2\bar{\zeta}} + \frac{a(3m_1^{1/2}-1)\bar{\zeta}}{2(m_1^{1/2}+1)} + \frac{2am_1^{1/2}(m_1^{1/2}-1)^2\bar{\zeta}^3}{3(m_1^{1/2}+1)^3} + \cdots, \tag{12}$$

where

$$\bar{\zeta} = \rho\exp(-i\theta), \quad 0 \le \rho \le 1, \quad -\pi \le \theta \le \pi. \tag{13}$$

Consequently, from (12) one infers on the slot boundary

$$\overline{\omega(\sigma)} = -\frac{a}{2}\sigma + \frac{a(3m_1^{1/2}-1)}{2(m_1^{1/2}+1)\sigma} + \frac{2am_1^{1/2}(m_1^{1/2}-1)^2}{3(m_1^{1/2}+1)^3\sigma^3} + \cdots \tag{14}$$

as $\bar{\sigma} = 1/\sigma$. Taking the first derivative of (12) with respect to $\bar{\zeta}$ produces

$$\bar{z}'(\bar{\zeta}) = \frac{a}{2\bar{\zeta}^2} + \frac{a(3m_1^{1/2}-1)}{2(m_1^{1/2}+1)} + \frac{2am_1^{1/2}(m_1^{1/2}-1)^2\bar{\zeta}^2}{(m_1^{1/2}+1)^3} + \cdots. \tag{15}$$

Because $\bar{\sigma} = 1/\sigma$, $\bar{z}'(\bar{\zeta})$ may be rewritten on the unit circle γ as

$$\overline{\omega'(\sigma)} = \frac{a}{2}\sigma^2 + \frac{a(3m_1^{1/2}-1)}{2(1+m_1^{1/2})} + \frac{2am_1^{1/2}(m_1^{1/2}-1)^2}{(1+m_1^{1/2})^3\sigma^2} + \cdots. \tag{16}$$

Let us now expand the function φ_0 of (9) in a power series in ζ of the form

$$\varphi_0(\zeta) = (b_1 + ic_1)\zeta + (b_3 + ic_3)\zeta^3 + \cdots, \tag{17}$$

where the various coefficients of the ζ expansion (b_1, c_1, b_3, c_3) are assumed to be real variables. On the unit circle γ, $\varphi_0(\zeta)$ becomes

$$\varphi_0(\sigma) = (b_1 + ic_1)\sigma + (b_3 + ic_3)\sigma^3 + \cdots. \tag{18}$$

Similarly, the complex conjugate of (17) is

$$\bar{\varphi}_0(\bar{\zeta}) = (b_1 - ic_1)\bar{\zeta} + (b_3 - ic_3)\bar{\zeta}^3 + \cdots, \tag{19}$$

with its first derivative being

$$\bar{\varphi}_0'(\bar{\zeta}) = (b_1 - ic_1) + 3(b_3 - ic_3)\bar{\zeta}^2 + \cdots . \tag{20}$$

On the unit circle boundary γ, $\bar{\varphi}_0'(\bar{\zeta})$ becomes

$$\overline{\varphi_0'(\sigma)} = (b_1 - ic_1) + \frac{3(b_3 - ic_3)}{\sigma^2} + \cdots . \tag{21}$$

The integrals of (10) can be evaluated using residue theory as all of the singularities that appear in the integrand are either simple or multiple poles.

The evaluation [Churchill 1960; Spiegel 1964] of an arbitrary integral in the complex plane having a single singularity at $z = z_0$ is

$$\int_\gamma f(z)\, dz = 2\pi i a_{-1}, \tag{22}$$

where a_{-1} is the residue at $z = z_0$. If multiple singularities arise within the unit circle γ, then the residue a_{-1} in (22) is simply replaced by the sum of the residues. It is assumed that the integral in (22) has no branch points. The residue a_{-1} can be determined for a simple pole by the following limit

$$a_{-1} = \lim_{z \to z_0} (z - z_0)\, f(z). \tag{23}$$

If a higher order pole exists at $z = z_0$, then the following alternative to (23) can be used

$$a_{-1} = \lim_{z \to z_0} \frac{1}{(n-1)!} \frac{d^{n-1}}{dz^{n-1}} [(z - z_0)^n f(z)], \quad n \geq 2, \tag{24}$$

where n is the order of the pole.

The residues of the integral on the left-hand side of (10) are evaluated at $\sigma = 0$ and $\sigma = \zeta$, as singularities exist there. In addition, residues are determined at the four roots of the following quartic equation in σ:

$$\sigma^4 + \frac{-1 + 3m_1^{1/2}}{1 + m_1^{1/2}} \sigma^2 + \frac{4m_1^{1/2}(-1 + m_1^{1/2})^2}{(1 + m_1^{1/2})^3} = 0, \tag{25}$$

which are explicitly

$$\sigma \longrightarrow \pm \frac{1}{\sqrt{2}} \sqrt{-3 + \frac{4}{1 + m_1^{1/2}} \pm \frac{\sqrt{1 - 7m_1^{1/2}(3 - 5m_1^{1/2} + m_1)}}{(1 + m_1^{1/2})^{3/2}}}. \tag{26}$$

The algebraic equation (25) is used to locate the roots of $\overline{\omega'(\sigma)} = 0$, which introduce singularities in the integrand, and consequently require evaluation using residue theory. All four of the roots (26) fall within the complex unit circle γ for $0 \leq m_1 \leq 1$, which is a necessary condition from residue theory for their inclusion in the evaluation.

The result of the evaluation of this integral by residue theory is

$$\frac{1}{2\pi i} \int_\gamma \frac{\omega(\sigma)}{\overline{\omega'(\sigma)}} \overline{\varphi_0'(\sigma)} \frac{d\sigma}{\sigma - \zeta} = \frac{4(b_1 - ic_1) m_1^{1/2} (-1 + m_1^{1/2})^2 \zeta}{3(1 + m_1^{1/2})^3}. \tag{27}$$

The subroutine for symbolic residue evaluation in Mathematica was used for determining the integral (27) in this example. Note that when numerical iteration is used for determining roots instead of an analytical expression, relationships (23) and (24) may have to be employed to determine the residues.

Similarly, the integral on the right-hand side of (10) requires residue evaluation at $\sigma = 0$ and $\sigma = \zeta$ producing the result

$$\frac{1}{2\pi i}\int_\gamma (f_1^0 + i f_2^0)\frac{d\sigma}{\sigma - \zeta} = -\frac{T_\infty a\zeta[-3 + 3e^{2ia}(1+m_1^{1/2})^3 + m_1^{1/2}[3 + 15m_1^{1/2} + 9m_1 + 4(-1+m_1^{1/2})^2\zeta^2]]}{12(1+m_1^{1/2})^3}. \quad (28)$$

By substituting (17), (27), and (28) into (10), one finds a relationship for determining the coefficients of the expansion of $\varphi_0(\zeta)$

$$aT_\infty\zeta\big[-3 + 3e^{2i\alpha}(1+m_1^{1/2})^3 + m_1^{1/2}[3 + 15m_1^{1/2} + 9m_1 + 4(m_1^{1/2}-1)^2\zeta^2]\big] + 12(1+m_1^{1/2})^3[(b_1 + ic_1)\zeta + (b_3 + ic_3)\zeta^3] + 16(b_1 - ic_1)m_1^{1/2}(m_1^{1/2}-1)^2\zeta = 0. \quad (29)$$

By setting the real and imaginary parts of the coefficients on ζ and ζ^3 individually equal to zero in (29), one determines the coefficients of the series as

$$b_1 = 3aT_\infty(1+m_1^{1/2})^2\left[\frac{1 - 3m_1^{1/2} - (1+m_1^{1/2})\cos 2\alpha}{4(3 + 13m_1^{1/2} + m_1 + 7m_1^{3/2})}\right], \quad (30)$$

$$c_1 = \frac{3aT_\infty(1+m_1^{1/2})^3 \sin 2\alpha}{4(-3 - 5m_1^{1/2} - 17m_1 + m_1^{3/2})}, \quad (31)$$

$$b_3 = -\frac{aT_\infty(-1+m_1^{1/2})^2 m_1^{1/2}}{3(1+m_1^{1/2})^3}, \quad c_3 = 0. \quad (32)$$

Now, a relationship established in [Muskhelishvili 1977] is

$$\sigma_\rho + \sigma_\theta = 4\,\mathrm{Re}\left[\frac{\varphi'(\zeta)}{z'(\zeta)}\right], \quad (33)$$

where σ_ρ and σ_θ are normal stresses in the ρ and θ directions. On the slot boundary, which is traction free, σ_ρ is zero so that (33) becomes [Savin 1961]

$$\sigma_\theta(\sigma) = 4\,\mathrm{Re}\left[\frac{\varphi'(\sigma)}{\omega'(\sigma)}\right]. \quad (34)$$

From (34) the stress concentration factor may be determined as the maximum principal stress will always be located on the surface of the slot.

This analysis is provided here only to demonstrate the basic technique used to generate the curves shown in Figures 2 and 3, whose analyses contain many more terms of ζ than the series (6). The series (6) was truncated after only three terms, as even a single additional term in the form of a fifth power of ζ would greatly increase the length of the solution presented for an arbitrary value of m_1.

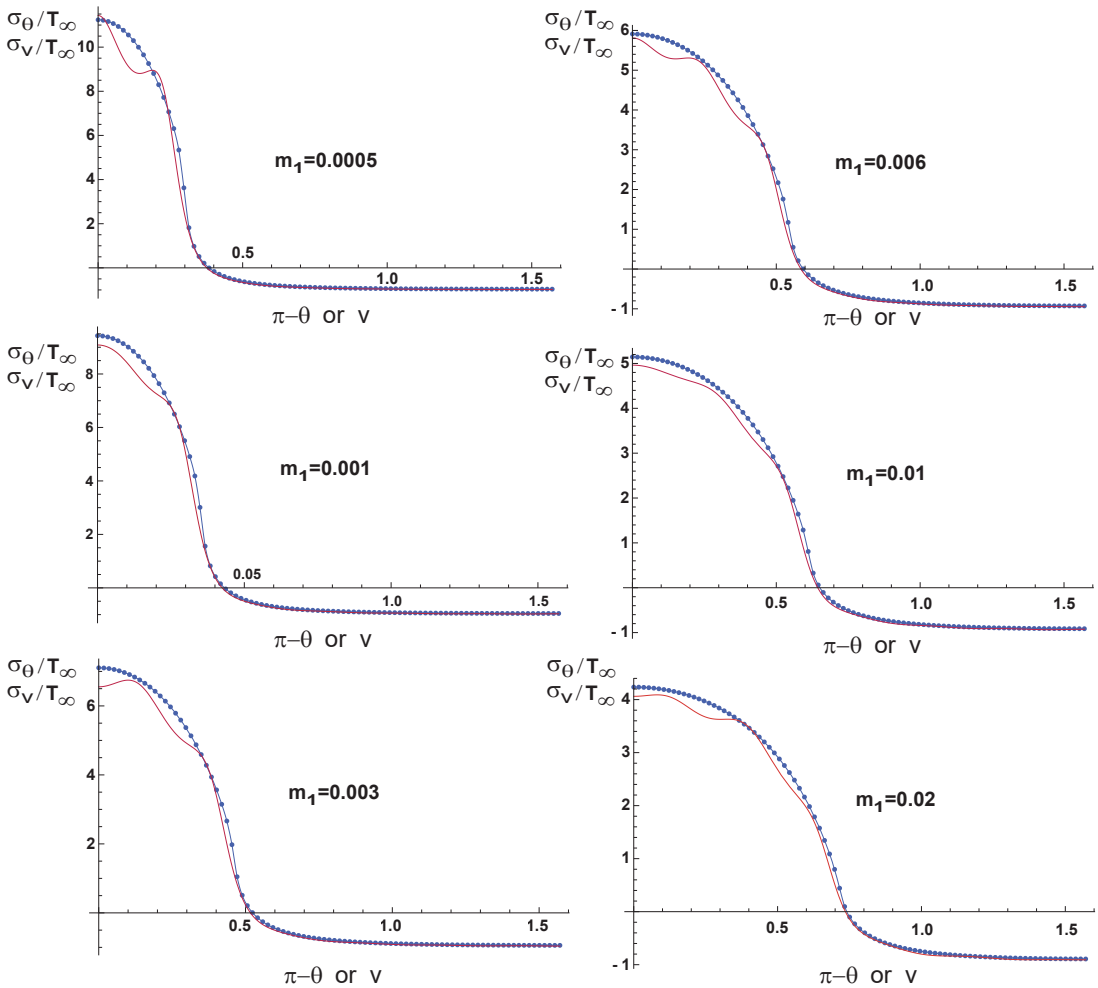

Figure 2. Stress distribution along slot surface under uniaxial loading for various slot aspect ratios (3).

All of the curves shown in Figures 2 and 3 were generated with expansions containing odd powers of ζ up to the twenty-third power using specific values of m_1. Two exceptions are also shown for the case $m_1 = 0.02$, where ζ was expanded only up to the twenty-first power.

The extreme length of these solutions preclude their being published in their entirety. Also note that finding roots of σ where singularities occur in the integrands often require numerical iteration for specific rather than arbitrary values of m_1. This was avoidable in the simple case of (25) because an analytical solution for the roots is possible (26) for arbitrary m_1. One must find all of the roots within the integrand of the integrals in (10) provided that the roots fall within the unit circle γ. This is necessary in order to evaluate the integrals in (10) using residue theory.

It is the curves showing oscillatory behavior in Figures 2 and 3 that were generated with this series expansion technique. The curves of Figure 2 were produced by taking $\alpha = \pi/2$, in (11), which corresponds to the direction of the remote tensile load T_∞ in the y-direction. The curves in Figure 3 were produced

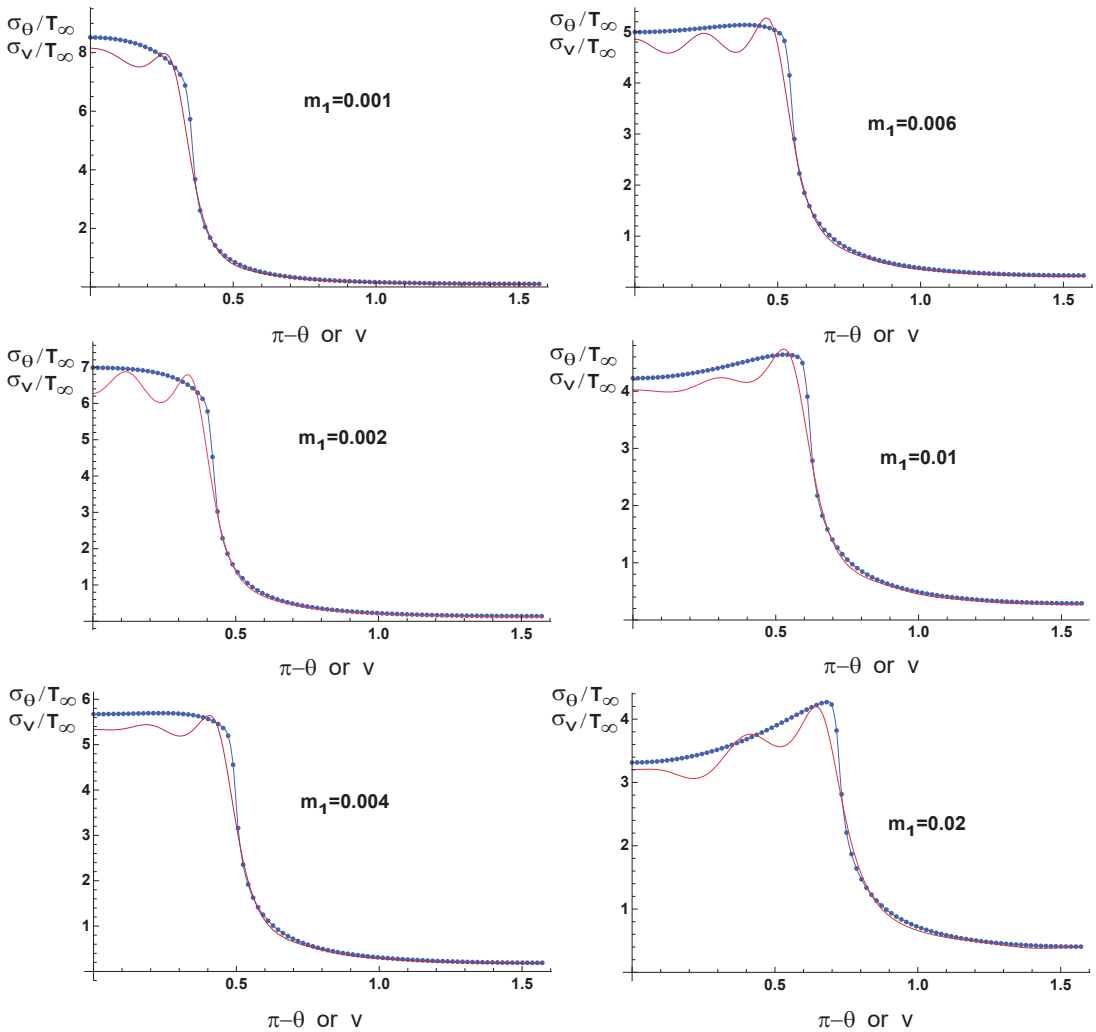

Figure 3. Stress distribution along slot surface under biaxial loading for various slot aspect ratios (3).

by superposing a solution with $\alpha = \pi/2$ to one with $\alpha = 0$ to simulate a uniform biaxial loading T_∞ of the plate at infinity.

The remaining curves of Figures 2 and 3 showing numerical data points joined by continuous curves were obtained from finite differences solutions, whose details are discussed in the following section.

3. Finite difference solutions of the slot problem

The isotropic plane stress linear elastic slot solution is determined in this section by finding an appropriate Airy stress function numerically. An Airy function $\phi = \phi(x, y)$ must solve the following fourth order

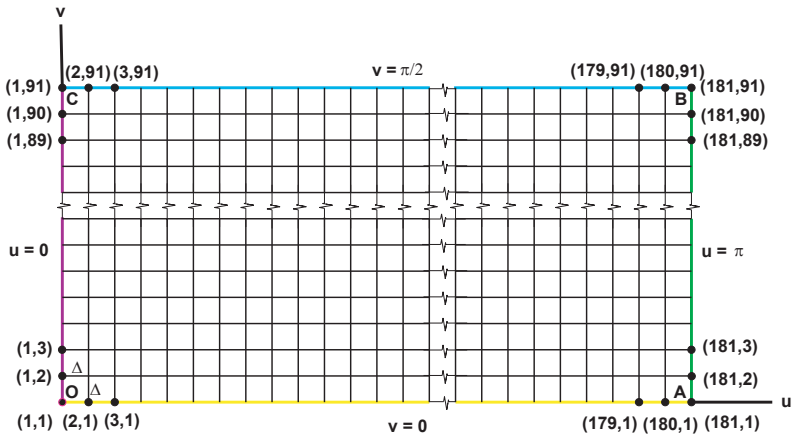

Figure 4. Square finite difference grid map of the curvilinear orthogonal coordinate system.

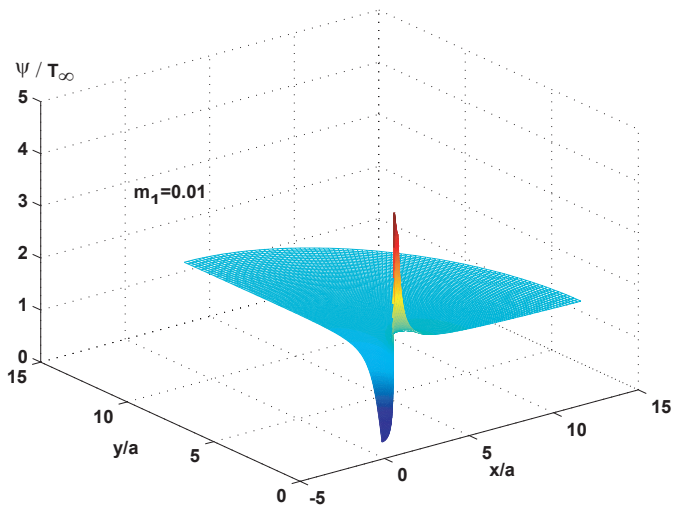

Figure 5. Sum of in-plane normal stresses ψ for biaxial loading.

partial differential equation, which is referred to as the biharmonic equation [Malvern 1969]

$$\nabla^4\phi = \nabla^4\phi(x, y) = \frac{\partial^4\phi(x, y)}{\partial x^4} + 2\frac{\partial^4\phi(x, y)}{\partial x^2\,\partial y^2} + \frac{\partial^4\phi(x, y)}{\partial y^4} = 0. \tag{35}$$

Equation (35) is valid provided that no body forces are present. The properties of the operator ∇^4 in (35) allow the biharmonic equation to be decomposed as

$$\nabla^4\phi = 0 \Longrightarrow \nabla^2(\nabla^2\phi) = 0 \Longrightarrow \nabla^2\psi = 0 \quad \text{for } \psi = \nabla^2\phi, \tag{36}$$

where the Laplacian operator ∇^2 is defined in Cartesian coordinates (x, y) by

$$\nabla^2(\,) = \frac{\partial^2(\,)}{\partial x^2} + \frac{\partial^2(\,)}{\partial y^2}. \tag{37}$$

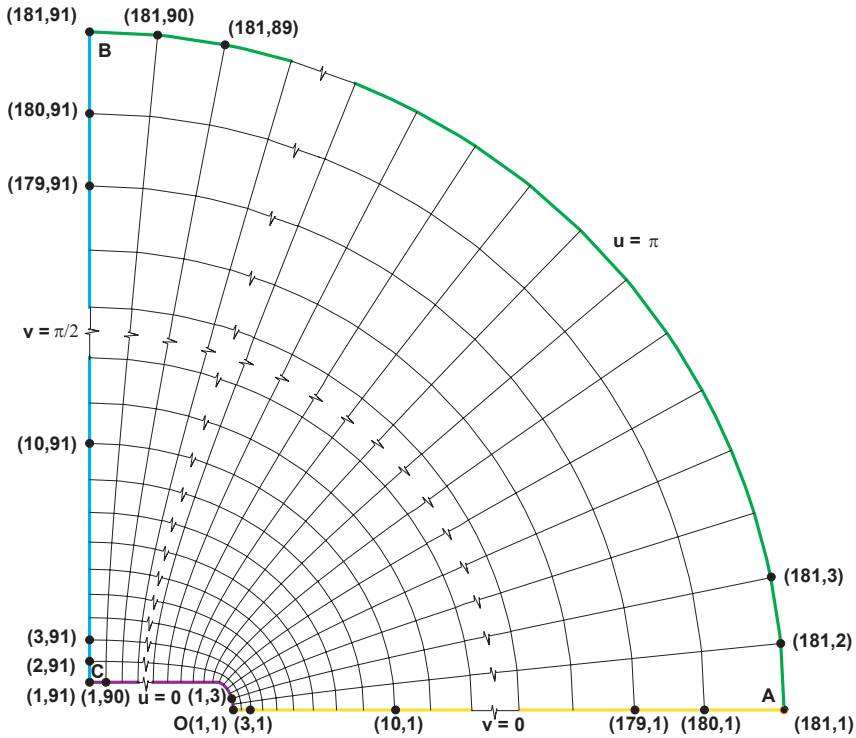

Figure 6. Curvilinear orthogonal coordinate system (u, v) of the slot problem.

The function ψ in (36) is referred to as a harmonic function indicating that it solves Laplace's equation

$$\nabla^2 \psi = 0. \tag{38}$$

By (36) the Airy function may also be thought of as solving Poisson's equation

$$\nabla^2 \phi = \psi. \tag{39}$$

Hence, a solution of the biharmonic equation may be decomposed into solving two second order partial differential equations simultaneously, (38) and (39), as noted previously in [Greenspan 1974].

The use of an orthogonal curvilinear system that naturally accommodates the slot geometry will greatly simplify the application of boundary conditions to the governing equation. A coordinate system closely related to (1) will be used here. Let us introduce the following substitution for ζ in (1):

$$\zeta = -\exp(-w), \quad \text{where } w = u + iv, \quad 0 \le u \le \infty, \quad -\pi \le v \le \pi. \tag{40}$$

A schematic drawing of this coordinate system (u, v) is shown in Figure 6 for the first quadrant of the xy plane. As $m_1 \to 0$, the coordinates u and v of (40) approach standard elliptical coordinates, where u is a family of confocal ellipses and v is a family of orthogonal hyperbolas. For a general value of m_1, the slot boundary is located at $u = 0$. On the slot boundary, the coordinate $\rho = 1$ so that $v = \pi - \theta$, as can be inferred from (5) and (40).

In the coordinate system defined by w, Poisson's equation (39) may be written as

$$\frac{\partial^2\phi}{\partial u^2}+\frac{\partial^2\phi}{\partial v^2}=h^2(u,v)\,\psi(u,v), \tag{41}$$

where the metric coefficient $h(u,v)$ in (41) can be determined using one of the following relationships:

$$h(u,v)=\sqrt{\frac{dz}{dw}\frac{d\bar{z}}{d\bar{w}}}=\sqrt{\mathrm{Re}^2(dz/dw)+\mathrm{Im}^2(dz/dw)}=\left|\frac{dz}{dw}\right|. \tag{42}$$

Laplace's equation (38) becomes in the new curvilinear system

$$\frac{\partial^2\psi}{\partial u^2}+\frac{\partial^2\psi}{\partial v^2}=0. \tag{43}$$

A nine-point finite difference scheme for Poisson's equation in [Rosser 1975], which also agrees with one in [Collatz 1960], is chosen for solution of (41) for interior nodes (i,j):

$$\begin{aligned}\phi_{i,j}=&\tfrac{1}{20}(\phi_{i-1,j+1}+\phi_{i+1,j+1}+\phi_{i-1,j-1}+\phi_{i+1,j-1})+\tfrac{1}{5}(\phi_{i,j+1}+\phi_{i-1,j}+\phi_{i+1,j}+\phi_{i,j-1})\\&-\frac{\Delta^2}{300}(82h^2_{i,j}\psi_{i,j}+h^2_{i-1,j+1}\psi_{i-1,j+1}+h^2_{i,j+1}\psi_{i,j+1}+h^2_{i+1,j+1}\psi_{i+1,j+1}+h^2_{i-1,j}\psi_{i-1,j}\\&+h^2_{i+1,j}\psi_{i+1,j}+h^2_{i-1,j-1}\psi_{i-1,j-1}+h^2_{i,j-1}\psi_{i,j-1}+h^2_{i+1,j-1}\psi_{i+1,j-1}),\end{aligned} \tag{44}$$

where Δ is the incremental change between adjacent nodes in the square mesh shown in Figure 4. The indices of the mesh range from $i=1$ to 181 and $j=1$ to 91.

Similarly, an equivalent formulation for the discretization of Laplace's equation (43) for interior nodes:

$$\psi_{i,j}=\tfrac{1}{5}(\psi_{i,j+1}+\psi_{i-1,j}+\psi_{i+1,j}+\psi_{i,j-1})+\tfrac{1}{20}(\psi_{i-1,j+1}+\psi_{i+1,j+1}+\psi_{i-1,j-1}+\psi_{i+1,j-1}). \tag{45}$$

Now the boundary condition for ψ along slot OC of Figure 6 must be derived. As the slot is traction free, the following relationships may be imposed [Malvern 1969] to satisfy this boundary condition:

$$\phi(0,v)=\left.\frac{\partial\phi}{\partial u}\right|_{u=0}=0. \tag{46}$$

As ϕ is constant along the slot by (46), the following relationships for partial derivatives of ϕ with respect to v and a reduction of Poisson's equation to an ordinary differential equation along the slot are deduced:

$$\left.\frac{\partial\phi}{\partial v}\right|_{u=0}=0\longrightarrow\left.\frac{\partial^2\phi}{\partial v^2}\right|_{u=0}=0\longrightarrow\frac{d^2\phi(0,v)}{du^2}=h^2(0,v)\,\psi(0,v). \tag{47}$$

Sixth order, forward, finite difference representations [Miller 1975] of partial derivatives of ϕ along the slot boundary $(i=1)$ follow

$$\begin{aligned}\left.\frac{\partial\phi}{\partial u}\right|_{1,j}&=0=\frac{1}{60\Delta}(-147\phi_{1,j}+360\phi_{2,j}-450\phi_{3,j}+400\phi_{4,j}-225\phi_{5,j}+72\phi_{6,j}-10\phi_{7,j}),\\\left.\frac{\partial^2\phi}{\partial u^2}\right|_{1,j}&=\frac{1}{180\Delta^2}(812\phi_{1,j}-3132\phi_{2,j}+5265\phi_{3,j}-5080\phi_{4,j}+2970\phi_{5,j}-972\phi_{6,j}+137\phi_{7,j}).\end{aligned} \tag{48}$$

In addition, from (46), one infers along the slot that

$$\phi(0, v) = \phi_{1,j} = 0 \quad \text{for } j = 1 \text{ to } 91. \tag{49}$$

From the ordinary differential equation in (47), combined with relationships (48) and (49), the discretized value of ψ along the slot boundary is

$$\psi_{1,j} = \frac{10\phi_{2,j} - 5\phi_{3,j} + 2.2222\phi_{4,j} - 0.625\phi_{5,j} + 0.08\phi_{6,j}}{h_{1,j}^2 \Delta^2}, \quad j \neq 1 \text{ or } 91. \tag{50}$$

Note that $\phi_{7,j}$ was chosen for elimination between equations (48) in the derivation of (50).

Equations (49) and (50) constitute the boundary conditions on ϕ and ψ respectively along slot OC of Figure 6 with the exception of the endpoints for ψ.

Other boundary conditions that must be satisfied along sides OA and BC of Figure 6 are due to symmetry

$$\text{OA and BC:} \quad \frac{\partial \phi}{\partial v} = 0, \quad \frac{\partial \psi}{\partial v} = 0. \tag{51}$$

The condition on ϕ defined by (51) was satisfied by employing simple forward and backward second order finite difference equations

$$\begin{aligned} &\text{OA:} \quad \phi_{i,1} = (4\phi_{i,2} - \phi_{i,3})/3, \qquad i \neq 1 \text{ or } 181, \\ &\text{BC:} \quad \phi_{i,91} = (4\phi_{i,90} - \phi_{i,89})/3, \quad i \neq 1 \text{ or } 181. \end{aligned} \tag{52}$$

The second boundary condition of (51) on ψ was combined with second order finite difference representations for Laplace's equation (43) in order to obtain the following relationships that are appropriate for homogeneous Neumann boundary conditions [Li and Lam 1964]

$$\begin{aligned} &\text{OA:} \quad \psi_{i,1} = (\psi_{i-1,1} + \psi_{i+1,1} + 2\psi_{i,2})/4, \qquad i \neq 1 \text{ or } 181, \\ &\text{BC:} \quad \psi_{i,91} = (\psi_{i-1,91} + \psi_{i+1,91} + 2\psi_{i,90})/4, \quad i \neq 1 \text{ or } 181. \end{aligned} \tag{53}$$

Along the exterior boundary AB, which represents infinity, two different types of loadings were considered. The first was for a uniaxial loading T_∞ in the direction of the y-axis (Figure 1). The second was for a uniform biaxial loading in the x and y directions. In the specific cases, the following relationships were used:

$$\begin{aligned} &\text{uniaxial loading on AB:} \quad \begin{cases} \phi_{181,j} = (T_\infty/2)\, x_{181,j}^2 \\ \psi_{181,j} = T_\infty, \end{cases} \qquad j = 1 \text{ to } 91, \\ &\text{biaxial loading on AB:} \quad \begin{cases} \phi_{181,j} = (T_\infty/2)(x_{181,j}^2 + y_{181,j}^2) \\ \psi_{181,j} = 2T_\infty, \end{cases} \qquad j = 1 \text{ to } 91. \end{aligned} \tag{54}$$

At the ends of the slot, points O and C respectively, second order finite difference representations of Laplace's equation were combined with second order finite difference equations of the second boundary condition of (51) to obtain

$$\psi_{1,1} = \psi_{3,1} + 2\psi_{1,2} - 2\psi_{2,1}, \quad \psi_{1,91} = \psi_{3,91} + 2\psi_{1,90} - 2\psi_{2,91}. \tag{55}$$

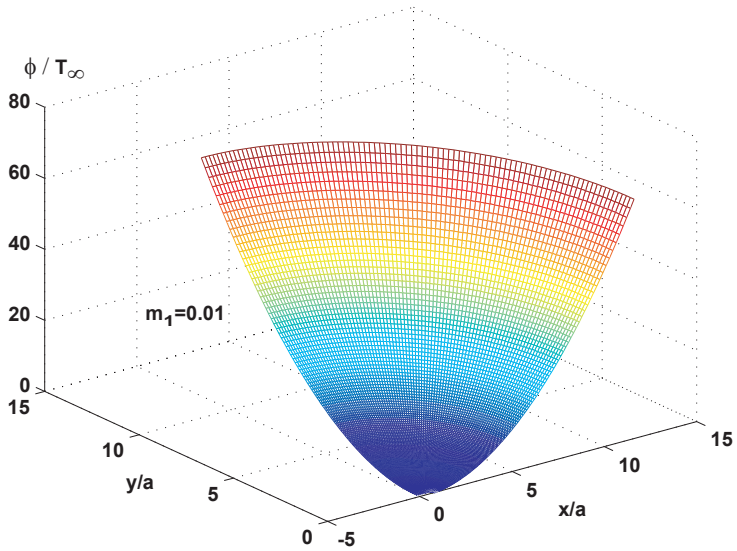

Figure 7. Airy stress function ϕ for biaxial loading.

A Jacobi iteration scheme [Akai 1994] was chosen to solve the governing equations for ϕ and ψ, (41) and (43) respectively, subject to boundary conditions (49), (50), (52)–(55). The value of the grid increment Δ used in the finite difference analysis was $\pi/180$. The value of u varied from 0 to π in the analysis, while the coordinate v varied from 0 to $\pi/2$. For $u = \pi$, there is approximately a one degree variation in the angle v between adjacent nodes in the physical plane. Representative plots of the solutions for ψ and ϕ for the biaxial loading case with $m_1 = 0.01$ are shown in Figures 5 and 7, respectively.

Note that

$$\psi = \sigma_x + \sigma_y = \sigma_u + \sigma_v, \tag{56}$$

where σ_x, σ_y, σ_u, and σ_v are normal stresses in their respective directions, which are designated by subscripts. On the slot boundary, σ_u is zero so that $\sigma_v = \psi$ by (56).

The MATLAB software was used for the numerical analysis. Subroutines for the evaluations of elliptic integrals for complex arguments were written by Igor Moiseev and downloaded from the MATHWORKS file exchange.

The convergence of the numerical scheme for the stress concentration factor for the uniaxial case of loading for a value of $m_1 = 0.01$, representing an infinite boundary, is shown in Figure 8 as the outer radius of the boundary R is increased. The value of R was calculated at the coordinate $v = 0$. It was determined numerically that little variance occurred in K_t beyond the value $u = \pi$ as indicated in the figure. This value of R is also small enough to maintain numerical stability of the iterative process as ϕ grows concurrently large. The mesh size itself was chosen to be fine enough to provide accurate numerical results while at the same time minimizing computation time for convergence of the iterative solution.

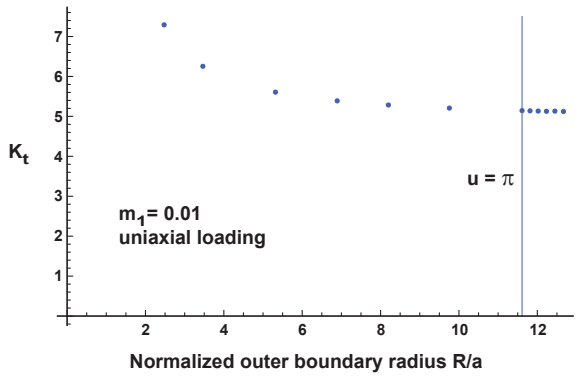

Figure 8. Convergence of numerical solution for stress concentration factor as a function of outer boundary radius.

4. Comparison of solutions

The numerical data points for various values of m_1 are shown in Figure 2 for a uniaxial tensile loading of the slot and in Figure 3 for a biaxial tensile loading of the slot. When the maximum principal stresses are plotted for the numerical data, fairly smooth curves connecting the data points are observed (Figure 9). In contrast, a plot of the maximum principal stresses for the series solutions would exhibit significant amounts of scatter in the data due to the oscillatory behavior of the solutions. On the other hand, there is still a discernable qualitative agreement between the series and the finite difference solutions plotted in Figures 2 and 3 along the slot surfaces. This fact lends additional support to the assumption that the boundaries representing infinity in the finite difference solutions are sufficiently distant from the origin that any additional length added to the existing boundary will have a negligible effect on the maximum principal stress.

An exact stress concentration factor K_t exists for the antiplane or mode III slot problem of this shape [Unger 2012a; 2012b; 2016; 2018; 2019]:

$$\text{antiplane shear loading:} \quad K_t = \tau_{\max}/\tau_\infty = 1/m_1^{1/4}, \tag{57}$$

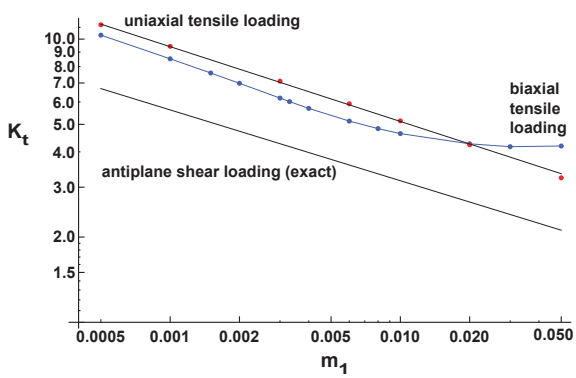

Figure 9. Stress concentration factor versus elliptic integral parameter.

where $\tau_{\max}$ is the largest equivalent shear stress and τ_∞ is the applied shear traction at infinity. Being a power law relationship, it appears as a straight line when plotted on the log-log scale of Figure 9. (Other authors who have found asymptotic solutions to semiinfinite slot problems with a cycloidal tip for a mode III loading are cited and discussed in [Unger 2012a; 2012b; 2018]).

A numerical fit to the data points for the uniaxial tensile loading case plotted in Figure 9 using the Mathematica software has the power law relationship

$$\text{uniaxial tensile loading:} \quad K_t = \sigma_v^{\max}/T_\infty = 1.52/m_1^{0.264}, \tag{58}$$

where $\sigma_v^{\max}$ is the maximum value of the normal stress σ_v in the v-direction. This value also corresponds to the maximum principal value of stress. The relationship (58) is plotted as a straight line through the uniaxial tensile data points in Figure 9. Combining (58) with (3) will allow a relationship between aspect ratio and the stress concentration factor to be generated. This simple power law relationship breaks down for values of m_1 greater than about 0.05. A plot of stress concentration factor versus slot aspect ratio is provided in Figure 10, which contains points having corresponding values of m_1 larger than 0.05. The value of slot aspect ratio corresponding to $m_1 = 0.05$ is approximately 1.88.

For the biaxial tensile loading, a transition occurs around $m_1 = 0.00316$ for the location of the maximum principal stress on the curved portion of the slot. For $m_1 \le 0.00316$, the largest principal stress occurs at the slot tip. For $m_1 > 0.00316$, the largest principal stress lies somewhere between the slot tip and the point where the flat surfaces begin. Figure 3 illustrates this behavior. The location of the coordinate v on the slot ($u = 0$) where the flat surfaces meet the rounded portions is

$$v = \cos^{-1}\frac{1 - m_1^{1/2}}{1 + m_1^{1/2}}. \tag{59}$$

A comparison is now made between the results obtained here for the case of the uniaxial tensile loaded slot of the type shown in Figure 1 to the work in [Bowie and Freese 1978] for a uniaxial tensile loaded ovaloid. Recall that the ovaloid is linear slot cut into a plate having semicircular ends. Thus the geometry of the ovaloid is very similar to the slot geometry addressed in this paper. It should also provide a qualitative check on the accuracy of the analysis presented here.

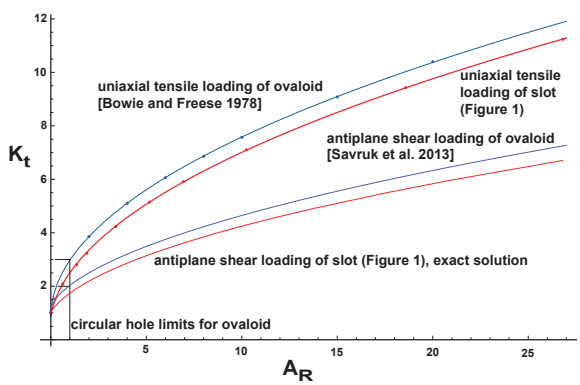

Figure 10. Comparison of stress concentration factor versus aspect ratio for two elongated holes.

The present author [Unger 2016] generated a continuous and smooth curve fit to the data points generated in [Bowie and Freese 1978] of the form

$$K_t = 0.850 + 2.13\sqrt{A_R}. \tag{60}$$

Note that this expression becomes invalid for values of stress concentration factor lower than a value of three as the ovaloid degenerates to a circular hole at that particular value.

A similar fit to the data points shown in Figure 9 for the uniaxial tensile loading of the slot together with a few additional data points covering the low aspect ratio region is

$$K_t = 0.324 + 2.11\sqrt{0.0783 + A_R}. \tag{61}$$

Unlike the ovaloid expression (60), the relationship (61) is valid down to an aspect ratio of zero where the shape of the slot degenerates to a vertical line that is parallel to the direction of load.

By comparing the two curves representing (60) and (61) in Figure 10, one can infer that the slot shape of Figure 1 produces lower stress concentration factors K_t than the ovaloid for identical aspect ratios of the slot. This might be attributed to the fact that the ovaloid has a smaller radius of curvature at the slot tip than does those of Figure 1 for the same aspect ratio [Unger 2016]. The radius of curvature ρ_t for the slot tip corresponding to relationship (4) is given by

$$\rho_t = 2a\frac{m_1^{1/2}}{1 - m_1^{1/2}}. \tag{62}$$

The radius of curvature at the tip of the ovaloid is naturally determined as half the width of the slot because its ends are semicircular in shape.

Similarly, a curve fit to numerical data points generated for the antiplane shear loading of the ovaloid was provided in [Savruk et al. 2013; Savruk and Kazberuk 2017] as

$$K_t = 1.3442\sqrt{A_R} + \frac{1}{1 + 0.5249\sqrt{A_R}}. \tag{63}$$

In Figure 10, this relationship is compared to the exact solution for the slot of Figure 1. The exact formula is obtained by combining (3) with (57).

One notes from Figure 10 that for both uniaxial tensile loading and antiplane shear loading of the slot of Figure 1 have lower stress concentration factors than those of the ovaloid for identical aspect ratios.

5. Conclusions

The finite difference solutions for the slot problem addressed in this article produce more reliable values of stress concentration factor than do the series solutions.

While the slot shape addressed in this paper produces lower stress concentration factors than does the ovaloid for identical hole aspect ratios, the close proximity of the two curves for each individual case in Figure 10 suggests that the additional complication of milling the slot tip of the specified shape (4) is unjustified in most cases. For the antiplane slot problem, relationship (57) remains the only exact solution of its kind for comparison.

In closing, the material contained within this article may help experimentalists in the field of fracture mechanics to better determine the state of stress into which a crack propagates in a specimen.

References

[Abramowitz and Stegun 1964] M. Abramowitz and I. A. Stegun, *Handbook of mathematical functions with formulas, graphs, and mathematical tables*, National Bureau of Standards Applied Mathematics Series **55**, U.S. Government Printing Office, Washington, D.C., 1964.

[Akai 1994] T. J. Akai, *Applied numerical methods for engineers*, Wiley, New York, 1994.

[Bowie and Freese 1978] O. L. Bowie and C. E. Freese, "Analysis of notches using conformal mapping", pp. 69–134 in *Stress analysis of notch problems: stress solutions to a variety of notch geometries used in engineering design*, edited by G. C. Sih, Mechanics of fracture **5**, Sijthoff & Noordhoff, Alphen aan den Rijn, 1978.

[Churchill 1960] R. V. Churchill, *Complex variables and applications*, McGraw-Hill, New York, 1960.

[Collatz 1960] L. Collatz, *The numerical treatment of differential equations*, 3rd ed., Springer, Berlin, 1960.

[Collins 1993] J. Collins, *Failure of materials in mechanical design: analysis, prediction, prevention*, 2nd ed., Wiley, New York, 1993.

[Creager and Paris 1967] M. Creager and P. C. Paris, "Elastic field equations for blunt cracks with reference to stress corrosion cracking", *Int. J. Fract. Mech.* **3**:4 (1967), 247–252.

[Greenspan 1974] D. Greenspan, *Discrete numerical methods in physics and engineering*, Mathematics in Science and Engineering **107**, Academic Press, New York, 1974.

[Hardy and Malik 1992] S. J. Hardy and N. H. Malik, "A survey of post-peterson stress concentration factor data", *Int. J. Fatigue* **14**:3 (1992), 147–153.

[Li and Lam 1964] W.-H. Li and S.-H. Lam, *Principles of fluid mechanics*, Addison-Wesley, Reading, 1964.

[Malvern 1969] L. E. Malvern, *Introduction to the mechanics of a continuous medium*, Prentice-Hall, Englewood Cliffs, 1969.

[Miller 1975] R. E. Miller, "Boundary value problems for mechanics", Class notes, TAM 493, University of Illinois at Urbana-Champaign, 1975.

[Muskhelishvili 1977] N. I. Muskhelishvili, *Some basic problems of the mathematical theory of elasticity*, 2nd ed., Noordhoff International Publishing, Leiden, 1977.

[Neuber 2001] H. Neuber, *Kerbspannungslehre*, 4th ed., Springer, Berlin, 2001.

[Pilkey et al. 2020] W. D. Pilkey, D. F. Pilkey, and Z. Bi, *Peterson's stress concentration factors*, 4th ed., Wiley, Hoboken, 2020.

[Riabouchinsky 1921] D. Riabouchinsky, "On steady fluid motions with free surfaces", *Proc. London Math. Soc.* **s-19**:1 (1921), 206–215.

[Rice 1988] R. C. Rice, *Fatigue design handbook*, Society of Automotive Engineers, Warrendale, 1988.

[Rosser 1975] J. B. Rosser, "Nine-point difference solutions for Poisson's equation", *Comput. Math. Appl.* **1**:3-4 (1975), 351–360.

[Savin 1961] G. N. Savin, *Stress concentration around holes*, Pergamon Press, Oxford, 1961.

[Savruk and Kazberuk 2017] M. P. Savruk and A. Kazberuk, *Stress concentration at notches*, Springer, 2017.

[Savruk et al. 2013] M. P. Savruk, A. Kazberuk, and G. Tarasyuk, "Stress concentration near holes in the elastic plane subjected to antiplane deformation", *Mater. Sci.* (*Russia*) **48**:4 (2013), 415–426.

[Spiegel 1964] M. R. Spiegel, *Complex variables with an introduction to conformal mapping and its applications including 640 solved problems*, McGraw-Hill, New York, 1964.

[Tada et al. 2000] H. Tada, P. C. Paris, and G. R. Irwin, *The stress analysis of cracks handbook*, 3rd ed., ASME Press, New York, 2000.

[Unger 2011] D. J. Unger, *Analytical fracture mechanics*, Dover, Mineola, 2011.

[Unger 2012a] D. J. Unger, "Linear elastic solutions for slotted plates", *J. Elasticity* **108**:1 (2012), 67–82.

[Unger 2012b] D. J. Unger, "Erratum to: linear elastic solutions for slotted plates", *J. Elasticity* **108**:1 (2012), 83.

[Unger 2016] D. J. Unger, "Linear elastic solutions for slotted plates revisited", pp. 2042–2043 in *Proc. of XXIV International Congress of Theoretical and Applied Mechanics*, 2016.

[Unger 2018] D. J. Unger, "Free streamline hydrodynamic analogy for a linear elastic antiplane slot problem with perfectly plastic ligaments at its ends", *J. Elasticity* **132**:2 (2018), 261–270.

[Unger 2019] D. J. Unger, "Visualizing the crack driving force through fluid analogy", *J. Mech. Behav. Mater.* **28**:1 (2019), 89–94.

[Vigdergauz 2006] S. Vigdergauz, "The stress-minimizing hole in an elastic plate under remote shear", *J. Mech. Mater. Struct.* **1**:2 (2006), 387–406.

Received 27 Dec 2019. Revised 30 Mar 2020. Accepted 18 Apr 2020.

DAVID J. UNGER: du2@evansville.edu
Department of Mechanical and Civil Engineering, University of Evansville, 1800 Lincoln Avenue, Evansville, IN 47722, United States